Fractionation of iron and chromium isotopes in hydrothermal plumes from the northern Mid-Atlantic Ridge

Journal: *Earth and Planetary Science Letters*

Wenhao Wang[1], Alastair J.M. Lough[1], Heather Goring-Harford[1], Oli Flanagan[1], David González-Santana[2], Joseph Resing[3], Douglas Connelly[4], Maeve C. Lohan[1], Alessandro Tagliabue[5], Rachael H. James[1]

[1] School of Ocean and Earth Science, University of Southampton, Southampton, SO14 3ZH, UK

[2] Institut Universitaire Européen de la Mer, Université de Bretagne Occidental, Plouzané, F-29280, France

[3] Joint Institute for the Study of the Atmosphere and Ocean, University of Washington, Seattle, WA 98115, US

[4] Marine Geosciences, National Oceanography Centre, Southampton, SO14 3ZH, UK

[5] Department of Earth, Ocean and Ecological Sciences, University of Liverpool, Liverpool, L69 3GP, UK

ww1n15@southamptonalumni.ac.uk

Abstract

Hydrothermal venting impacts the global-scale biogeochemical cycles of many trace metals and their isotopes. Processes in hydrothermal plumes regulate the dispersal of vent-derived metals and

may vary in response to differences in the geologic setting of vent fields and/or the geochemistry of the overlying ocean water. Here we present results of analyses of dissolved Fe and Cr concentrations, and dissolved Fe isotope (δ^{56}Fe) and Cr isotope (δ^{53}Cr) distributions, in seawater samples collected from above TAG and Rainbow vent sites on the Mid-Atlantic Ridge during the GEOTRACES GA13 cruise. We show that profiles of dissolved Fe and Cr isotopes through the near-field hydrothermal plumes are the mirror image of each other. Oxidation of Fe(II) and precipitation of Fe-(oxyhydr)oxides account for the low δ^{56}Fe values of dissolved Fe, as low as −1.83‰ at TAG and −6.94‰ at Rainbow. Plume samples with low δ^{56}Fe values are associated with elevated δ^{53}Cr values of dissolved Cr compared to background seawater (by up to +0.14‰ and +0.69‰ at TAG and Rainbow, respectively), while particulate Cr is characterised by relatively low δ^{53}Cr values (−1.02 to −1.22‰). This striking result suggests that seawater Cr(VI) is reduced to Cr(III) and precipitates on the surface of Fe(III) particles within the hydrothermal plume. Reduction of Cr(VI) and scavenging of Cr(III) by plume Fe-(oxyhydr)oxide particles mean that high-temperature hydrothermal systems are likely a net sink for seawater Cr at Rainbow (and also at TAG). As the removal flux of Cr is related to the flux of hydrothermal Fe(II) and the rate of Fe(II) oxidation in the hydrothermal plume, it may (i) vary across vent sites at a global scale and (ii) change over glacial-interglacial cycles.

Key words: iron isotopes, chromium isotopes, hydrothermal plume, TAG, Rainbow, GEOTRACES

1 Introduction

Although hydrothermal fluids are highly enriched in metals relative to ambient seawater, chemical processes in hydrothermal plumes modify fluxes of metals into the wider ocean and may even result in net removal of some elements from seawater (e.g., *German et al., 1991*). As some metals, such as iron (Fe), are important micronutrients, it is essential to have a proper understanding of chemical processes in hydrothermal plumes to assess the impacts of hydrothermal inputs on the ocean metal inventory (*Tagliabue et al., 2014*).

The stable isotope compositions of Fe and Cr (δ^{56}Fe and δ^{53}Cr) are emerging tools for assessing the provenance of metal inputs to the ocean, and for exploring the effects of redox processes. For example, the heterogeneous distribution of δ^{56}Fe values of dissolved Fe has been shown to reflect input of Fe from dust dissolution (δ^{56}Fe ~+0.68‰; *Conway and John, 2014*), reductive and non-reductive release of Fe from marine sediments (δ^{56}Fe = −3.3 to −1.8‰ and ~+0.07‰, respectively: *Homoky et al., 2009; Homoky et al., 2021*), and hydrothermal venting (end-member vent fluid δ^{56}Fe = −0.67‰ to −0.12‰: e.g., *Severmann et al., 2004; Rouxel et al., 2008; Bennett et al., 2009; Klar et al., 2017; Nasemann et al., 2018; Wang et al., 2021*); the balance between abiotic removal and remineralization further shapes Fe isotope distributions in the ocean interior (*König et al., 2021*). δ^{53}Cr values of dissolved Cr in the open ocean range from +0.6 to +1.7‰ (e.g., *Scheiderich et al., 2015; Goring-Harford et al., 2018; Moos and Boyle, 2019; Rickli et al., 2019; Moos et al., 2020; Janssen et al., 2020; Nasemann et al., 2020; Huang et al., 2021; Janssen et al., 2021; Janssen et al., 2023; Wang et al., 2023*) and there appears to be an inverse relationship between logarithmic Cr concentration and δ^{53}Cr (e.g., *Scheiderich et al., 2015*). This relationship can be attributed, in part, to partial reduction of Cr(VI), which is highly soluble as the chromate (CrO_4^{2-}) ion in oxic seawater, to Cr(III), which is relatively insoluble and particle reactive, in surface waters

and oxygen minimum zones (*Scheiderich et al., 2015*). Reduction of Cr(VI) can be facilitated by the presence of Fe(II), Fe(II)-bearing minerals and organic matter, and is accompanied by a relatively large Cr isotope fractionation: $\delta^{53}Cr_{Cr(VI)} - \delta^{53}Cr_{Cr(III)}$ of up to 4.2‰ (e.g., *Døssing et al., 2011; Kitchen et al., 2012*).

While the Fe isotopic signature of seawater has proved useful for distinguishing between inputs of Fe from atmospheric deposition and seafloor sediments, the $\delta^{56}Fe$ of hydrothermal vent fluids is known to change as vent fluids mix with seawater (*Conway and John, 2014; Klar et al., 2017; Lough et al., 2017; Fitzsimmons et al., 2017; Nasemann et al., 2018; Wang et al., 2021*) as steep gradients in temperature, pH and Eh lead to substantial precipitation of Fe as sulfides and (oxyhydr)oxides (*Mottl and McConachy, 1990; Rudnicki and Elderfield, 1993*). Nevertheless, a fraction of hydrothermal Fe can persist in the water column, likely sustained by dissolved-particulate exchange (*Fitzsimmons et al., 2017; Tagliabue et al., 2022*), and is stabilised in the form of organic complexes and/or nanoparticles (e.g., *Toner et al., 2009; Fitzsimmons et al., 2017; Findlay et al., 2019; Wang et al., 2022*). Hydrothermal Cr, presumably in its reduced form (*Huang et al., 2019*), can also precipitate as vent fluids mix with seawater (*Trocine and Trefry, 1988; German et al., 1991)*. In addition, Cr(VI) in ambient seawater may be partly reduced to Cr(III) by reductants originating from vent fluids and subsequently scavenged onto particles (*Bauer et al., 2019; Jeandel and Minster, 1984*). In support of this, hydrothermal sediments at the southern East Pacific Rise have been reported to have lower $\delta^{53}Cr$ value compared to seawater (*Bauer et al., 2019*). However, the influence of hydrothermal venting on Cr and $\delta^{53}Cr$ distributions at regional or global scales is not clear (*Jeandel and Minster, 1984*; *Janssen et al., 2023*).

To better understand the processes that regulate the ridge-derived fluxes of Fe, Cr and their isotopes as they are dispersed through hydrothermal plumes, seawater samples were collected from

above the Trans-Atlantic Geotraverse (TAG) and the Rainbow vent fields on the northern Mid-Atlantic Ridge (MAR), during the GEOTRACES GA13 cruise (Figure 1a). Our data indicate that seawater $\delta^{56}Fe$ and $\delta^{53}Cr$ values are significantly modified in the hydrothermal plume and they provide evidence for coupled cycling of Fe and Cr isotopes. The implications of this result for interpretation of the Cr isotope redox proxy are also discussed.

2. Sampling sites

The Trans-Atlantic Geotraverse (TAG) vent field is located at 26°08′ N 44°50′ W and a depth of ~3650 m, at the base of the eastern wall of the rift valley of the slow-spreading MAR. Hosted in basaltic rocks, the TAG vent field consists of a series of high temperature (>360°C) black smokers that are clustered together close to the apex of a large sulfide mound. The end-member vent fluids have pH >3, Fe concentration of 5.0-5.6 mM, manganese (Mn) concentration of 0.68-0.73 mM, and H_2S content of 3-4 mM (*Chiba et al., 2001*).

The Rainbow vent field is located at 36°14′ N 33°54′ W and ~2310 m depth, at the western end of a non-transform discontinuity cutting across the MAR south of the Azores. The Rainbow vent field is hosted in ultramafic rocks (mainly serpentinised peridotite) and contains high temperature (~365°C) black smokers. In comparison to TAG, the Rainbow vent fluids are characterised by low pH (2.8), high chlorinity (750 mM), high H_2 (16 mM) and abundant organic compounds (*Douville et al., 2002*). The fluids also have higher Fe (24 mM) and lower H_2S (1.2 mM) concentrations (*Douville et al., 2002*). The lower pH, high concentrations of organic compounds, and high Fe are likely related to serpentinisation reactions (*Douville et al., 2002*).

Hydrographically, the TAG vent field is overlaid by waters that mainly consist of Denmark Strait Overflow Water (DSOW), Classical Labrador Sea Water (CLSW), and Antarctic Bottom Water (AABW); water overlying the Rainbow vent field mainly consists of CLSW (Figure 1b). Note that DSOW, CLSW, Upper Labrador Sea Water (ULSW), and Iceland-Scotland Overflow Water (ISOW) all contribute to North Atlantic Deep Water (NADW). At both vent sites, the hydrothermal plumes rise several hundred meters into the water column before they attain neutral buoyancy and disperse laterally.

3 Methods

3.1 Sample collection

Samples for this study were collected on board the RRS *James Cook* (JC156 cruise) as part of the UK GEOTRACES North Atlantic GA13 transect between 20th of December 2017 and 1st of February 2018, using pre-cleaned 10 L Ocean Test Equipment (OTE) water sampling bottles that were mounted on a titanium rosette system. On recovery, the OTE bottles were transferred into a trace metal clean container for sub-sampling. Seawater was filtered through a Sartobran 300 (Sartorius) filter capsule (0.2 µm) or a polyethersulfone filter (PES, Supor, Pall Gelman, 0.45 µm) under gentle pressure, and was collected into acid-cleaned low-density polyethylene (LDPE) bottles. The PES filter was placed in a pre-cleaned petri slide following filtration and was frozen at −20°C until particulate metal analysis. Filtered seawater samples for the analysis of dissolved trace metals (dMe) and isotopes were preserved by adding UpA-grade hydrochloric acid (HCl, *Romil*) to 0.024 M immediately after collection, and were stored for several months before the isotope analysis.

A Seabird 911 plus conductivity, temperature and depth (CTD) profiler system together with a light scattering sensor (LSS) and an oxidation-reduction potential (ORP) sensor were also attached to the titanium rosette. The hydrothermal plume above the vent fields was identified by a positive LSS and a negative ORP signal (Figure 1; *Lough et al., 2023*). The TAG plume was sampled at water column depths of between ~3100 and 3500 m, and was classified as the neutrally-buoyant plume based on the absence of a density anomaly over this depth interval. At Rainbow, plume signals were recorded from close to the seafloor to up to ~1800 m water depth; the buoyant part of the plume was likely captured at water depths of between ~2100 and 2200 m based on a negative density (and positive temperature) anomaly over this interval (Figure S1). Multiple CTD sampling casts were carried out at both TAG (CTD 76, 78) and Rainbow (CTD 36, 43) in order to collect enough water for all chemical analyses.

3.2 Dissolved Fe and Cr isotope analysis

All acids used for chemical processing were thermally distilled. De-ionised (Milli-Q) water was used for diluting and for cleaning. LDPE bottles and Perfluoroalkoxy (PFA) vials were thoroughly acid-cleaned for trace metal purposes. Samples were handled under laminar flow hoods, set within Class 100 clean laboratories at the National Oceanography Centre Southampton.

The Fe isotope composition of seawater samples was determined using a ^{57}Fe-^{58}Fe double spike technique, as described in *Lough et al. (2017)* and *Wang et al. (2021)*. Samples of between ~100 mL and 2 L volume were pre-concentrated using NTA Superflow resin and were then purified by anion exchange chromatography using AG-MP1 resin (BioRad). The Cr isotope composition was determined using a ^{50}Cr-^{54}Cr double spike method described in *Goring-Harford et al. (2018)* and *Wang et al. (2023)*. Cr in seawater samples of ~1 L to 2 L volume was co-precipitated with Fe(II)

hydroxide. Cr was then separated from the Fe by anion exchange chromatography (BioRad AG1-X8), and further purified by processing through a cation exchange (BioRad AG50W-X12) column. The purified Fe or Cr samples were evaporated to dryness and re-dissolved in 0.3 M (Fe) or 0.45 M (Cr) HNO_3 for analysis of their isotope ratios. Full details of the analytical procedures are given in Supplementary Information S1.

The isotopic compositions of Fe and Cr were determined by multicollector inductively coupled plasma mass spectrometry (MC-ICP-MS; Thermo Scientific Neptune Plus) at the University of Southampton. Raw data were blank corrected and corrected for mass bias using an iterative deconvolution procedure. The final Fe or Cr isotope values of the samples are reported in delta notation relative to international isotope standards (IRMM-14 for Fe and NBS979 for Cr) and expressed as:

$$\delta^{56}Fe\ (‰) = [(^{56}Fe/^{54}Fe)_{sample}/(^{56}Fe/^{54}Fe)_{IRMM\text{-}14} - 1] \times 1000 \quad (1)$$

$$\delta^{53}Cr\ (‰) = [(^{53}Cr/^{52}Cr)_{sample}/(^{53}Cr/^{52}Cr)_{NBS979} - 1] \times 1000 \quad (2)$$

The precision and accuracy of the methods were assessed through the analysis of: (1) trace metal free seawater doped with hematite (HEM) Fe isotope standard, (2) Black Sea Fe GEOTRACES intercomparison 'anoxic' sample, (3) OSIL Atlantic salinity standard seawater (for Cr), and (4) Beaufort Sea Cr inter-laboratory cross-calibration samples. Results of these analyses and comparisons with values reported in the literature or by other groups for these materials are shown in Table S1. We apply ±0.10‰ and ±0.06‰ as the external reproducibility (2σ) for $\delta^{56}Fe$ and $\delta^{53}Cr$, respectively, for all samples in this study, based on repeat analyses of the HEM (Fe) and the OSIL (Cr) samples (see Table S1). The Fe or Cr concentration of each sample was determined simultaneously with the isotope ratios using isotope dilution equations, based on the known sample volume and the quantity of added spike; we apply 2% uncertainty (2σ) for the measured Fe and Cr

concentrations (Supplementary Information S1). All dissolved Fe and Cr data are given in Tables S2 and S3.

3.3 Particulate Fe and Cr analysis

Subsamples of particulate material representing half of the 25 mm diameter 0.45 µm PES filters were processed following recommended GEOTRACES protocols (*Cutter et al, 2017*). The PES filters were thoroughly cleaned with 1.2 M HCl and Milli-Q water (Supplementary Information S3) prior to passing up to ~6 L (Table S4) of seawater through the filter on board the ship.

Filter halves were refluxed in a 1 mL solution of 50% HNO_3 and 10% HF (v/v, Optima Grade, Romil) at 135°C for 4h, evaporated to near dryness, and re-dissolved in 3 mL of 5% HNO_3 solution (spiked with 1 ppb In). Metal concentrations were determined by HR-ICP-MS (Element XR, Thermo Scientific) at the University of Southampton. Instrument drift was corrected using the 1 ppb In spike and element concentrations were obtained by calibration against a 10-point multi-element standard. The certified reference material BCR-414 was taken through the same digestion procedure as a check on the recovery of trace metals (Cr >82%, Fe >96%; n=1). Filter blanks (0.95-7.3 ng for Fe, 0.88-1.13 ng for Cr, per half filter) were negligible relative to the mass of the sample for Fe (<1%), but can represent up to 48% of the filter particulate load for Cr (Table S4). For this reason, only filters with >40 ng Cr were analysed for $\delta^{53}Cr$ to ensure the effect of the blank was minimal (Figure S2).

Sample digests (from two depths within the Rainbow plume) were purified utilising the same anion and cation column procedure as used for dissolved Cr, and Cr isotope ratios were then determined

198 by MC-ICP-MS (Neptune Plus) as described in Section 3.2. Particulate Fe and Cr data are given
199 in Table S4.

200

201 **3.4 Ancillary analyses**

202 Seawater samples were also collected for the analysis of total dissolvable Fe (TDFe) concentration.
203 These samples were unfiltered, and acidified with UpA-grade HCl (Romil) to 0.024 M; thus TDFe
204 consists of both dissolved Fe and Fe from the labile fraction of suspended particles. In a clean
205 laboratory, concentrations of TDFe (as well as dFe that is reported in the GEOTRACES IDP
206 database; Table S2) were determined by HR-ICP-MS (Element XR, Thermo Scientific) using a
207 standard addition method as described in *Lough et al. (2023)*. Measurements of dissolved Fe(II)
208 concentrations were made on board the ship by FIA-CL immediately after collection of the
209 samples (*González-Santana et al., 2023*). The Fe(II) samples were filtered either inline or prior to
210 analysis with a 0.2 µm syringe filter, and buffered inline to pH ~5.5 prior to pre-concentration on
211 a column filled with 8-hydroxyquinoline (8-HQ) chelating resin. Dissolved manganese (Mn)
212 concentrations were determined on board by flow injection analysis with inline pre-concentration
213 on resin-immobilized 8-HQ and colorimetric detection (*Resing and Mottl, 1992*). Excess helium
214 (xs^3He), which represents the mantle derived ^3He, was also determined (*Lough et al., 2023*).

215 The measured TDFe and dFe(II) concentrations were used to support the Rayleigh fractionation
216 modelling (Section 5.1). The Mn concentrations were used to calculate the dilution factors for
217 waters within the hydrothermal plume. Mn shows near-conservative behaviour during mixing of
218 vent fluids and seawater and serves as a tracer of hydrothermal plume dispersal on the spatial
219 scales of this study (*Lough et al., 2023*). The vent fluid (VF) dilution factor can be determined
220 from the proportion of vent fluid derived Mn and seawater derived Mn in a water sample, i.e.

dilution factor = ($[Mn]_{VF}$ – $[Mn]_{SW}$) / ($[Mn]_{sample}$ – $[Mn]_{SW}$), where $[Mn]_{sample}$ is the measured sample Mn concentration, $[Mn]_{SW}$ is the Mn concentration of background seawater (~0.15 nM; *GEOTRACES IDP 2021*) and $[Mn]_{VF}$ is the Mn content of the end-member vent fluid (Table 1).

4 Results

Water column profiles of dissolved Fe (dFe) concentrations and dissolved Fe isotope composition above the TAG and the Rainbow vent fields are shown in Figure 2. The dissolved Fe and $\delta^{56}Fe$ profiles at the TAG station are consistent with those reported in a previous GEOTRACES study (*Conway and John, 2014*). Within the TAG plume, dFe concentrations were as high as 67.1 nmol kg^{-1} while $\delta^{56}Fe$ values of dFe were as low as −1.83‰. The Rainbow hydrothermal plume was characterised by elevated dFe concentrations of up to 58.7 nmol kg^{-1} and very low $\delta^{56}Fe$ values of dFe, as low as −6.94‰. The Fe isotope compositions of the TAG and Rainbow end-member vent fluids were reported to be −0.15‰ and −0.14‰, respectively (*Severmann et al., 2004*), indicating that Fe sourced from the vent fluid is isotopically fractionated as the vent fluids mix with ambient seawater.

In contrast to Fe, dissolved Cr (dCr) was slightly depleted in the hydrothermal plumes compared to ambient seawater; the lowest concentration at TAG was 2.62±0.05 nmol kg^{-1}, compared to a background value of ~2.75±0.25 nmol kg^{-1}, and the lowest concentration at Rainbow was 2.13±0.04 nmol kg^{-1}, compared to a background value of ~2.47±0.25 nmol kg^{-1}. Note our methodology for estimating background values is provided in Figure 3. Samples from hydrothermal plumes also had elevated $\delta^{53}Cr$ values of dCr compared to ambient seawater, up to $\delta^{53}Cr$ = +1.23±0.06‰ (background ~+1.09±0.10‰) and $\delta^{53}Cr$ = +1.87±0.06‰ (background

~+1.18±0.10‰), respectively, at TAG and Rainbow. The 'mirror image' of dissolved Fe and Cr isotope profiles (Figure 2) provides evidence for coupled cycling of Fe and Cr in the hydrothermal plume.

Suspended particles in the hydrothermal plume were enriched in Fe and Cr compared to overlying seawater (Figure 2). Particulate Fe (pFe) concentrations were as high as 187 nM in the TAG plume and were up to 3770 nM in the Rainbow plume. Particulate Cr (pCr) concentrations measured in the plume were 17-171 pM and 149-1110 pM, respectively, at TAG and Rainbow. There was a positive correlation between pFe and pCr concentrations at both sites (r^2 = 0.89 and 0.98, respectively; Figure 4 and Table S4). The δ^{53}Cr of pCr from the Rainbow hydrothermal plume was determined to be −1.02 and −1.22‰ at depths of 2051 m and 2108 m, respectively. Because of the low pCr concentrations, it was not analytically feasible to determine the δ^{53}Cr of pCr in the TAG plume.

5 Discussion

5.1 Fe isotope behaviour in the hydrothermal plume

When Fe- and H_2S-rich vent fluids come into contact with seawater, some of the Fe immediately precipitates, most likely as Fe-sulfide (FeS and FeS_2; *Mottl and McConachy 1990; Rudnicki and Elderfield, 1993*). Kinetic fractionation of Fe isotopes during Fe-sulfide precipitation would leave the residual dissolved Fe enriched in heavier iron isotopes (estimated $\delta^{56}Fe_{FeS} - \delta^{56}Fe_{dFe} = -0.60$‰: *Butler et al., 2005; Bennett et al., 2009*). The effects of precipitation of vent fluid Fe as sulfide can be examined using a Rayleigh fractionation model:

$$\delta^{56}Fe = (\delta^{56}Fe_{VF} + 1000) \cdot f^{\alpha_0 - 1} - 1000 \quad (3)$$

where $\delta^{56}Fe_{VF}$ is the Fe isotope composition of the end-member vent fluid, α_0 is the fractionation factor between FeS and Fe(II) (~0.9994; given by $\alpha_0 \approx e^{\delta^{56}Fe_{FeS} - \delta^{56}Fe}$), and f is the proportion of Fe remaining in the plume. Given that Fe-sulfides mostly form large aggregates (>20 μm) and settle out of the plume rapidly (e.g., *Lough et al., 2017; Findlay et al., 2019*), the f value can be estimated by the ratio of the measured to the calculated total Fe concentration in the hydrothermal plume:

$$f = \frac{[\mathrm{TDFe}]_{\mathrm{meas}}}{[\mathrm{Fe}]_{\mathrm{VF}} \,/\, [\text{VF dilution factor}]} \quad (4)$$

where $[TDFe]_{meas}$ is the concentration of total dissolvable Fe measured in the sample, $[Fe]_{VF}$ is Fe content in the end-member vent fluid (VF), and the VF dilution factor can be determined from the proportion of Mn content of the sample (see Section 3.4). According to this calculation, the proportion of Fe lost via precipitation as Fe-sulfide during the earliest stages of mixing between the hydrothermal fluid and seawater was 29±9% (1σ, n=3) at TAG and 9±12% (1σ, n=4) at Rainbow (Table 1). These estimates are generally consistent with the vent fluid Fe/H_2S stoichiometry: vent fluids from Rainbow have higher Fe/H_2S (~20) compared to TAG vent fluids (~1.5) (*Severmann et al., 2004*), so a greater proportion of Fe remains in solution. Loss of Fe at TAG is nevertheless slightly lower than expected from vent fluid Fe/H_2S stoichiometry, possibly due to formation of nanoparticulate pyrite that is preserved in the dissolved fraction (*Gartman et al., 2014*). According to Equation 3, the $\delta^{56}Fe$ value of hydrothermal Fe that remains and is transported further into the hydrothermal plume, beyond the immediate Fe-sulfide precipitation stage, is calculated to be 0.06±0.07‰ (1σ, n=3) and −0.08±0.08‰ (1σ, n=4), respectively, at TAG and Rainbow; corresponding Fe concentrations are ~159±53 (1σ, n=2) and 2020±950 (1σ, n=4) nM at the two sites (Table 1).

The $\delta^{56}Fe$ values of dFe in the hydrothermal plumes at both sites were much lower than the values calculated from Equation 3 (as low as −1.83‰ at TAG and −6.94‰ at Rainbow). Precipitation of Fe-(oxhyhydr)oxides (FeOOH) fractionates Fe isotopes; preferential incorporation of heavy Fe isotopes into FeOOH ($\delta^{56}Fe_{FeOOH} - \delta^{56}Fe_{dFe} \approx 3.5$‰ at a temperature of 3°C: *Welch et al., 2003; Wu et al., 2011*) and the subsequent aggregation of colloidal-sized (0.02 to 0.2 μm) FeOOH into particles (>0.2 μm) leave the Fe that remains in the dissolved fraction isotopically light. The theoretical oxidation half-life of Fe(II) is in the range of minutes to hours in ambient seawater above the TAG and Rainbow vent sites (*Field and Sherrell, 2000; González-Santana et al., 2021*). Thus, with continuous mixing of vent fluids and oxygenated seawater, the fractionation effect of FeS precipitation is overwritten by Fe(II)-Fe(III) oxidation. In addition, strong Fe-binding ligands, such as siderophores, exert controls on dFe concentrations in the TAG and Rainbow hydrothermal plumes; more than 99% of the dFe has been interpreted to be complexed by L1 ligands (*Hoffman et al., 2023*). Experiments indicate that ligand-bound Fe(III) (FeL) can be enriched in heavy Fe isotopes by up to 0.6‰ relative to inorganic Fe(III) (*Dideriksen et al. 2008; Morgan et al., 2010*).

$\delta^{56}Fe$ values of dFe in the hydrothermal plume can be modelled in terms of Rayleigh fractionation, as a function of the proportion (*F*) of dFe remaining as Fe(II) along with the proportion (*X*) of Fe(III) remaining in the dissolved (colloidal) fraction (*Klar et al., 2017; Lough et al., 2017; Nasemann et al., 2018; Wang et al., 2021*):

$$\delta^{56}\mathrm{Fe(II)} = (\delta^{56}\mathrm{Fe(II)}_0 + 1000) \cdot F^{\alpha_1 - 1} - 1000 \quad (5)$$

$$\delta^{56}\mathrm{Fe(III)} = (\delta^{56}\mathrm{Fe(II)}_0 + 1000) \cdot \frac{1 - F^{\alpha_1}}{1 - F} - 1000 \quad (6)$$

$$\delta^{56}\mathrm{FeL} = (\delta^{56}\mathrm{Fe(III)} + 1000) \cdot \frac{1 - X^{\alpha_2}}{1 - X} - 1000 \quad (7)$$

$$\delta^{56}Fe_{dFe} = \frac{F \cdot \delta^{56}Fe(II) + X \cdot (1-F) \cdot \delta^{56}FeL}{F + X \cdot (1-F)} \quad (8)$$

where $\delta^{56}Fe(II)_0$ is the initial isotopic composition of dissolved Fe (0.06‰ at TAG and −0.08‰ at Rainbow, accounting for the effects of Fe-sulfide precipitation), $\delta^{56}Fe(II)$ is the isotopic composition of the remaining Fe(II), $\delta^{56}Fe(III)$ is the Fe isotopic composition of inorganic Fe(III), $\delta^{56}FeL$ is the isotopic composition of ligand-bound Fe (note we assume that all Fe(III) remaining in the dissolved fraction is complexed with ligands, consistent with *Hoffmann et al. (2023)*, and there is no re-equilibration between Fe(II) and FeL), and α_1 is the fractionation factor between inorganic Fe(III) and aqueous Fe(II) (~1.0035; given by $\alpha_1 \approx e^{\delta^{56}Fe(III) - \delta^{56}Fe(II)_{aq}}$), α_2 is the fractionation factor between FeL and inorganic Fe(III) (~1.0006; given by $\alpha_2 \approx e^{\delta^{56}FeL - \delta^{56}Fe(III)}$).

The results of this modelling exercise are illustrated in Figure 5. The observed low $\delta^{56}Fe$ values of dFe in the TAG and Rainbow hydrothermal plumes are consistent with a substantial degree of Fe(II) oxidation and FeOOH precipitation. This result is consistent with calculations based on measured concentrations of dFe(II), dFe and TDFe (Table 1). Assuming that Fe-(oxyhydr)oxides have relatively small particle sizes and tend to remain in the plume (e.g., *Fitzsimmons et al., 2017; Tagliabue et al., 2022; Lough et al., 2023*), then *F* and *X* values can be estimated as follows:

$$F = \frac{[dFe(II)]}{[TDFe]} \quad (9)$$

$$X = \frac{[dFe] - [dFe(II)]}{[TDFe] - [dFe(II)]} \quad (10)$$

The proportion of Fe remaining as Fe(II) in the plume is calculated to be ~4-7% (n=4) at TAG and ~0.1-0.4% (n=4) at Rainbow, and the proportion of Fe(III) remaining in the dissolved fraction is ~25-53% (n=4) and ~1-4% (n=4) at the two sites respectively (Table 1).

Differences in δ^{56}Fe values of dissolved Fe between the two sites are largely driven by differences in the degree of dissolved Fe that precipitates as Fe-(oxhyhydr)oxide. Relative to TAG, Rainbow vent fluids have higher Fe concentrations and higher Fe/H_2S, so after the initial Fe-sulfide precipitation stage more Fe is available for Fe-(oxyhydr)oxide formation. In addition, the rate of Fe(II) oxidation by O_2 is higher in the Rainbow plume than it is in the TAG plume (*Field and Sherrell, 2000; González-Santana et al., 2021*). All these factors point to a higher loading of Fe-(oxyhydr)oxide particles in the Rainbow plume which, in turn, increases the rate of aggregation of colloidal FeOOH (e.g., *Fitzsimmons et al., 2015*). As a result, near quantitative (>99%) precipitation and removal of Fe occurs in the Rainbow hydrothermal plume, resulting in the lowest δ^{56}Fe value for dissolved Fe in seawater reported to date (−6.94‰). These new data support the idea that vent fluid chemistry and the chemistry of bottom seawater can, in part, control the δ^{56}Fe signature of dFe delivered to the hydrothermal plumes and potentially into the ocean interior (e.g., *Rouxel et al., 2016; Lough et al., 2017; Wang et al., 2021*). This is an important consideration for utilising Fe isotopes to constrain the relative importance of different external sources of Fe to the oceans (*Conway and John, 2014; König et al., 2021*) and, in turn, is critical for providing reliable predictions of future changes in the distribution of Fe and other micronutrients as well as carbon export (*Tagliabue et al., 2014; König et al., 2021*).

5.2 Cr isotope behaviour in the hydrothermal plume

The first measurements of the Cr isotope composition of hydrothermal fluids have recently been reported for high temperature (~300 °C) and high Fe:H_2S (up to >10; *Kleint et al., 2019*) vent fluids from the dacite-hosted Brothers Volcano at the Kermadec Arc. The δ^{53}Cr value of the fluids ranged from −0.17 to +0.08‰ (*Janssen et al., 2023*), similar to the range reported for igneous

rocks ($\delta^{53}Cr$ = −0.12±0.10‰; *Schoenberg et al., 2008*). End-member Cr concentrations in the Brothers Volcano vent fluids (8 to 27 nmol kg^{-1}; *Janssen et al., 2023*) and vent fluids from mafic- and ultramafic-hosted hydrothermal systems (up to ~640 nmol kg^{-1}; *Evans et al., 2023*) (see also Supplementary Information S4) are relatively low compared to other metals, consistent with the limited solubility of reduced species of Cr in hydrothermal fluids (*Huang et al., 2019*). The molar Cr/Fe ratio of freshly precipitated particles determined in this study is 8.7±1.5 × 10^{-4} at TAG and 3.0±0.2 × 10^{-4} at Rainbow (determined from the slope of the pCr/pFe correlation; Figure 4), similar to values reported previously for vent sites at TAG and the southern East Pacific Rise (~2 × 10^{-4} to ~5 × 10^{-4}: *German et al., 1991; Trocine and Trefry, 1988; Feely et al., 1996*). These ratios are ~1 to 3 orders of magnitude higher than the expected Cr/Fe ratio of TAG or Rainbow vent fluids (assuming end-member Cr concentrations of 10 to 640 nmol kg^{-1}). This comparison suggests that most of the particulate Cr is likely derived from ambient seawater (*Rudnicki and Elderfield, 1993*). Uptake of Cr from seawater onto hydrothermal plume particles is also supported by analysis of the chemical composition of metalliferous sediments from the southern East Pacific Rise (*Bauer et al., 2019*). The $\delta^{53}Cr$ value of the authigenic phase of these sediments is relatively low (as low as −1.2‰), which is consistent with partial reduction of Cr(VI) in ambient seawater and incorporation of the isotopically light Cr(III) that forms in metalliferous particles (*Bauer et al., 2019*).

Our data reveal that the dissolved Fe and Cr isotope profiles through the hydrothermal plume at both TAG and Rainbow are the mirror image of one another (Figure 2). This provides evidence for coupled Fe(II) oxidation and Cr(VI) reduction in the hydrothermal plume. In the presence of Fe(II) or Fe(II)-bearing minerals, seawater Cr(VI) can be partly reduced to Cr(III), which preferentially incorporates light Cr isotopes (e.g., *Døssing et al., 2011; Kitchen et al., 2012*). The Cr(III) can be subsequently scavenged by Fe-(oxyhydr)oxide particles (e.g., *Frei et al., 2009*),

leaving the Cr(VI) that remains in the dissolved fraction isotopically heavy. As the contribution of vent fluid Cr delivered to the plume is expected to be minimal (<0.08 nmol kg^{-1} for the least dilute plume sample, assuming similar end-member Cr concentrations to Main Endeavour (*Evans et al., 2023*)), the evolution of dissolved $\delta^{53}Cr$ in the hydrothermal plume due to reduction of Cr(VI) and removal of the Cr(III) that forms can be described in terms of a closed-system Rayleigh process:

$$\delta^{53}Cr_{dCr} = (\delta^{53}Cr_{sw} + 1000) \cdot p^{\alpha-1} - 1000 \quad (11)$$

where SW is background seawater (Section 4 and Figure 3), α is the fractionation factor between Cr(III) and Cr(VI) ($\alpha \approx e^{\delta^{53}Cr(III) - \delta^{53}Cr(VI)}$), and p is the proportion of Cr remaining in the dissolved fraction given by:

$$p = \frac{dCr}{[Cr]_{sw}} \quad (12)$$

Figure 5 shows that the measured Cr data in the hydrothermal plume can be primarily explained by the Rayleigh model, whereby the Cr isotope fractionation factor between Cr(III) and Cr(VI) is estimated from the correlation between the logarithmic dCr concentration and $\delta^{53}Cr$ (~−2.0±1.1‰ for TAG and −4.5±1.4‰ for Rainbow). Experimentally determined fractionation factors for reduction of Cr(VI) by ferrous Fe are in the range of −3.60‰ to −4.20‰ (*Døssing et al., 2011; Kitchen et al., 2012*), whilst Fe(II)-bearing minerals, such as FeS and green rust, are thought to show more muted fractionation (−1.50‰ to −2.65‰: *Døssing et al., 2011; Basu and Johnson, 2012*). Similarly, the fractionation factor between Cr(III) in the authigenic phase of metalliferous sediments and Cr in seawater for the southern East Pacific Rise has been estimated to be between −0.80‰ and −2.65‰ (*Bauer et al., 2019*). Thus, our estimated fractionation factors agree with both the experimental and the field data. The lower fractionation factor determined for TAG may indicate that Fe-sulfide particles exert a greater control on Cr reduction, either as Fe-sulfides

initially precipitate or possibly at a later stage as Fe-sulfide nanoparticles coagulate. The high Fe/H_2S ratio in Rainbow hydrothermal fluids means that a larger proportion of Fe(II) oxidises and precipitates as (oxyhydr)oxides at this site.

The previously proposed 'global correlation' between the Cr concentration and $\delta^{53}Cr$ value of seawater samples is consistent with Rayleigh-type fractionation of Cr isotopes in the open ocean characterised by a single fractionation factor (~−0.80‰, *Scheiderich et al., 2015*; Figure 6), but there is ongoing discussion as to the underlying process(es) that regulate this relationship (e.g., *Huang et al., 2021; Janssen et al., 2021; Wang et al., 2023*). It is now generally accepted that although Cr is partly reduced in the euphotic zone due to biological and/or photochemical processes (e.g., *Janssen et al., 2020*), as well as in the OMZs by organic matter, microbial activity, and possibly Fe(II) (*Moos et al., 2020; Nasemann et al., 2020; Huang et al., 2021*), the intrinsic Cr isotope fractionation is diminished as a portion of isotopically light Cr(III) remains in the dissolved phase (*Moos et al., 2020; Nasemann et al., 2020; Huang et al., 2021*); it is also plausible that regeneration of Cr from sinking particles along the deep water thermohaline flow path plays a role (*Wang et al., 2023*). Our full water column Cr data at the TAG station yield an overall fractionation factor of −0.88‰, which is consistent with the 'global correlation', but it is clear from Figure 6 that the hydrothermal plume samples at Rainbow have anomalously high $\delta^{53}Cr$ values compared to the 'global correlation' line. Similar anomalously high $\delta^{53}Cr$ values ($\delta^{53}Cr$ up to +3.85 and +4.15‰) were observed in seawater samples collected from within 30 m of the seafloor on the Chukchi shelf (*Moos, 2018*); these were primarily attributed to reduction of seawater Cr by Fe(II) diffusing from the reducing shelf sediments.

According to the Rayleigh model, the $\delta^{53}Cr$ value of particulate Cr(III) in the hydrothermal plume is predicted to be isotopically light compared to seawater Cr(VI) if the reduction is not quantitative

(Figure 5). For the two Rainbow plume samples that have the highest dissolved $\delta^{53}Cr$ values, the measured $\delta^{53}Cr$ values of particulate Cr were −1.02 and −1.22‰. These values are somewhat higher than predicted (~−3.0‰; Figure 5), possibly due to incorporation of seabed particles entrained in the rising plume near the seafloor (*Lough et al., 2023*). Nevertheless, plume particles will eventually be deposited in metalliferous sediments, confirming that negative Cr isotope excursions are indicative of hydrothermal activity as previously hypothesised for sediments from the Pacific and the proto-North Atlantic (*Holmden et al., 2016; Bauer et al., 2019; Yobo et al., 2022*). Note that diagenetic oxidation of hydrothermal Cr(III) precipitates can further deplete sediments in ^{53}Cr (*Bauer et al., 2019*).

5.3 Coupled cycling of Fe and Cr in the hydrothermal plume and wider implications for oceanic Cr and Cr isotope budgets

Figure 2 provides evidence that Cr is removed from seawater in the hydrothermal plume, indicating that hydrothermal activity at Rainbow (and possibly at TAG) is a net sink, rather than a source, of Cr in the ocean. The hydrothermal removal flux of Cr for the global ocean can be estimated from the Cr deficit in the plume (0.08±0.04 nmol kg^{-1} (1σ, n=6) at TAG and 0.20±0.09 nmol kg^{-1} (1σ, n=5); Section 5.2) and the estimated volume of the oceans that passes through the hydrothermal plume each year (1.8-3.4 × 10^{17} kg yr^{-1}, assuming an entrainment ratio of ~10^4 at the height of neutral buoyancy: *Elderfield and Schultz, 1996*). Extrapolating our TAG and Rainbow data to the global scale, this method yields a mean Cr removal flux from the oceans of 1.5±0.8 to 6.9±3.1 × 10^7 mol yr^{-1}. This is consistent with earlier work at TAG (4.8 × 10^7 mol yr^{-1}; *Rudnicki and Elderfield, 1993*) that estimated the Cr flux based on measured particulate Cr/Fe ratios and available Fe-(oxyhydr)oxides that scavenge Cr. Compared to the estimated total input fluxes of Cr

to the oceans (8.77×10^8 mol yr^{-1}: *Pöppelmeier et al., 2021*), the hydrothermal removal flux of Cr calculated in this way is relatively small (~2 to 8% of the input flux) but non-negligible. Note, however, that several caveats need to be considered (see below).

Cr(III) could be re-oxidised in a catalytic reaction with MnO_x, but this process is likely negligible in the proximal hydrothermal plume given the very slow rates of Cr oxidation (*van der Weijden and Reith, 1982*). Culture experiments suggest that coupled Mn(II) and Cr(III) oxidation by marine Mn(II)-oxidising bacteria can be much more rapid, with a half-life for Cr oxidation of a few hours (*Miletto et al., 2021*). However, there is little evidence for oxidation of Mn(II) to MnO_x in the plumes at TAG and Rainbow over the spatial scales of our sampling, as dissolved Mn shows (near-)conservative behaviour and is linearly correlated with excess ^{3}He (*Lough et al., 2023*). Furthermore, onboard incubations of plume samples showed constant dMn concentrations over a period of >3 weeks (*Lough et al., 2023*).

Based on our Cr and Fe isotope data, we propose that removal of Cr occurs via reduction of seawater Cr(VI), with Fe(II) or Fe(II)-bearing minerals as the electron donor, and scavenging of Cr(III) onto the surface of the Fe(III)-(oxyhydr)oxides that form (Figure 7). The rate law for Cr(VI) reduction with Fe(II) in oxygenated seawater, including a decay term for Fe(II) that accounts for possible oxidation of Fe(II) by O_2 (*Pettine et al., 1998*), is:

$$-\frac{\mathrm{dCr(VI)}}{\mathrm{dt}} = k_{\mathrm{Cr}}\,[\mathrm{Cr(VI)}]\,[\mathrm{Fe(II)} \cdot \mathrm{e}^{-k_{\mathrm{Fe}}\,[\mathrm{O_2}]\,[\mathrm{OH^-}]^2\,\mathrm{t}}] \quad (13)$$

where the rate constants k_{Cr} and k_{Fe} are a function of pH, temperature and ionic strength (Supplementary Information S5), and the initial Fe(II) concentration is estimated based on the mean TDFe concentration in the hydrothermal plume (Section 5.1 and Table 1). Modelled decay curves for the reduction of Cr(VI) by Fe(II) in the TAG and Rainbow hydrothermal plumes are

shown in Figure 8. The model demonstrates that as the initial concentration of Fe(II) is well in excess of Cr concentrations in seawater, and the rate of Fe(II) oxidation by O_2 is slower than the rate of Cr(VI) reduction by Fe(II), then reduction of Cr(VI) with Fe(II) results in observable loss of dCr from the plume, which is consistent with our observations. The rate of Cr loss is principally dependent on the initial Fe(II) concentration and the rate of Fe(II) oxidation and the Cr concentration plateaus once oxidation of Fe(II) is close to complete. Although the rate of Fe(II) oxidation by O_2 is slightly lower in the TAG plume (Supplementary Information S5; *González-Santana et al., 2021*), as the concentration of Fe(II) initially delivered to the Rainbow plume is much higher than the concentration delivered to the TAG plume, the amount of dCr lost from seawater by reduction of Cr(VI) with Fe(II) is higher at Rainbow than it is at TAG. Note that the time scale for Cr(VI) reduction is much shorter than the estimated residence time of Fe-oxyhydr(oxide) particles in the plume (>300 days at TAG; *Rudnicki and Elderfield, 1993*), so levels of Fe-(oxydr)oxides are not expected to be the limiting factor for Cr scavenging/removal.

These results have several implications for interrogation of δ^{53}Cr records in marine sediments. Firstly, studies of the Cr isotope record of atmospheric oxygenation preserved in authigenic marine sediments rely on the assumption that Cr(VI) is efficiently reduced to Cr(III) with Fe(II), such that the sediments record the δ^{53}Cr value of seawater (e.g., *Frei et al., 2009; Crowe et al., 2013*). While the applicability of the Cr isotope proxy has been questioned because processes in addition to oxidative weathering have been shown to produce heavy Cr isotope enrichment in weathering solutions (e.g., ligand promoted dissolution of Cr(III)-(hydr)oxides (*Saad et al., 2017*); overprinting of the primary δ^{53}Cr signal (*Albut et al., 2018*)), our data further reveal that in the presence of oxygen, Cr(VI) may not always be quantitatively reduced to Cr(III) with Fe(II).

Incomplete reduction and removal of Cr has also been observed above the chemocline in a redox-stratified lake (*Janssen et al., 2022*).

Secondly, as the removal flux of Cr is related to both the vent fluid chemistry (flux of hydrothermal Fe(II)) and chemistry of bottom seawater (the rate of Fe(II) oxidation in the plume), it will vary from site to site. For example, at Brothers Volcano and the Snakepit hydrothermal vent site on the MAR (*Janssen et al., 2023; Wang et al., 2023*), no clear depletion (or enrichment) of dCr in hydrothermally influenced seawater has been observed. If the Cr decay model is applied to the Southern East Pacific Rise (SEPR) (Supplementary Information S5), reduction of Cr is negligible because of limited supply of Fe(II) even though the rate of Fe(II) oxidation is relatively slow (Figure S3). These observational and modelling results suggest that large uncertainties remain when extrapolating Cr deficits at TAG and Rainbow to the global scale. Moreover, possible variations in vent fluid Cr concentrations as well as diagenetic oxidation of hydrothermal Cr(III) precipitates (*Bauer et al., 2019*) that may partly release Cr back into the water column also need to be considered.

Finally, changes in the hydrothermal removal flux of Cr could be sufficient to impact seawater δ^{53}Cr. For example, removal of Cr may have been higher during the Last Glacial Maximum due to (1) enhanced hydrothermal input of Fe related to rapid sea level changes (e.g., *Middleton et al., 2016*), and/or (2) depressed Fe(II) oxidation rates in the hydrothermal plume (*Cullen and Coogan, 2017*). Increased removal of Cr in the plume would lead to higher seawater δ^{53}Cr values that have previously been interpreted to reflect periods of globally increased productivity and expanded marine anoxia (e.g., *Gueguen et al., 2016*).

6 Conclusions

This study investigated how chemical processes in hydrothermal plumes regulate hydrothermal inputs of Fe and Cr to the ocean interior by utilising a novel stable isotope approach at two vent sites on the Mid-Atlantic Ridge. We show for the first time that profiles of dissolved Fe and Cr isotopes through hydrothermal plumes are the 'mirror image' of one another, providing evidence for coupled Fe(II) oxidation and Cr(VI) reduction. Oxidation of Fe(II) and precipitation of Fe-(oxyhydr)oxides in the hydrothermal plume account for the low δ^{56}Fe values of dissolved Fe, as low as −1.83‰ at TAG and −6.94‰ at Rainbow. The latter represents the lowest δ^{56}Fe value for dFe in seawater reported to date; differences in δ^{56}Fe values between the two sites are largely driven by the differences in the degree of oxidation of Fe(II) and precipitation of Fe-(oxyhydr)oxides. Reduction of seawater Cr(VI) is implied by elevated δ^{53}Cr values of dissolved Cr in the hydrothermal plumes compared to background seawater by, respectively, up to ~+0.14‰ and +0.69‰ at TAG and Rainbow. In support of this, plume particles have relatively low δ^{53}Cr values (−1.02 to −1.22‰ at Rainbow). The estimated Cr isotope fractionation factor for reduction of Cr(VI) with Fe(II) ($\delta^{53}Cr_{Cr(III)} - \delta^{53}Cr_{Cr(VI)}$) is −4.5±1.4‰ at Rainbow, significantly greater than that calculated for the 'global correlation' between seawater Cr concentration and δ^{53}Cr in the open ocean. Reduction of Cr and scavenging by Fe-(oxyhydr)oxide particles in the hydrothermal plume mean that high-temperature hydrothermal systems are possibly a net sink for seawater Cr, potentially removing up to ~8% of the total input flux of Cr to the ocean. Changes in hydrothermal Fe fluxes and ocean chemistry (that influences the rate of Fe(II) oxidation) also have the potential to cause significant shifts in seawater δ^{53}Cr that need to be considered for accurate interpretation of the Cr isotope redox proxy.

Acknowledgements

We thank the captain and crew of the RRS James Cook and the JC156 shipboard scientific party for all their assistance during the JC156/GA13 cruise. The cruise was supported by the NERC-funded FeRidge project (NE/N010396/1 and NE/N009525/1). We thank Sharon Walker (NOAA/PMEL) for providing the ORP and optical backscatter sensors. WW's PhD studentship was funded by the Chinese Scholarship Council and the Graduate School of National Oceanography Centre Southampton. OF was funded by a NERC-INSPIRE PhD award (NE/S007210/1). DGS received funding from ISblue project, Interdisciplinary graduate school for the blue planet (ANR-17-EURE-0015), and from the French government under the program 'Investissements d'Avenir'. JR was funded by NOAA Ocean Exploration and Earth-Ocean Interactions programs through the Cooperative Institute for Climate, Ocean, and Ecosystem Studies; this is CICOES contribution #2023-1271 and PMEL contribution #5521. The international GEOTRACES programme is partly supported by a US National Science Foundation grant (OCE-1840868) to the Scientific Committee on Oceanic Research (SCOR). We also thank David Janssen, an anonymous reviewer, and the associate editor Laurence Coogan, for their constructive comments.

References

Albut, G., Babechuk, M.G., Kleinhanns, I.C., Benger, M., Beukes, N.J., Steinhilber, B., Smith, A.J.B., Kruger, S.J., Schoenberg, R., 2018. Modern rather than Mesoarchaean oxidative weathering responsible for the heavy stable Cr isotopic signature of the 2.95 Ga old Izermijn iron formation (South Africa). *Geochimica et Cosmochimica Acta*, 228, 157-189.

Basu, A., Johnson, T.M., 2012. Determination of hexavalent chromium reduction using Cr stable isotopes: isotopic fractionation factors for permeable reactive barrier materials. *Environmental Science & Technology*, 46(10), 5353-5360.

Bauer, K.W., Cole, D.B., Asael, D., Francois, R., Calvert, S.E., Poulton, S.W., Planavsky, N.J., Crowe, S.A., 2019. Chromium isotopes in marine hydrothermal sediments. *Chemical Geology*, 529, 119286. DOI: 10.1016/j.chemgeo.2019.119286

Bennett, S.A., Rouxel, O., Schmidt, K., Garbe-Schönberg, D., Statham, P.J., German, C.R., 2009. Iron isotope fractionation in a buoyant hydrothermal plume, 5°S Mid-Atlantic Ridge. *Geochimica et Cosmochimica Acta*, 73(19), 5619-5634.

Butler, I.B., Archer, C., Vance, D., Oldroyd, A., Rickard, D., 2005. Fe isotope fractionation on FeS formation in ambient aqueous solution. *Earth and Planetary Science Letters*, 236(1), 430-442.

Chiba, H., Masuda, H., Lee, S.Y., Fujioka, K., 2001. Chemistry of hydrothermal fluids at the TAG active mound, MAR 26°N, in 1998. *Geophysical Research Letters*, 28(15), 2919-2922.

Conway, T.M., John, S.G., 2014. Quantification of dissolved iron sources to the North Atlantic Ocean. *Nature*, 511(7508), 212-215.

Crowe, S.A., Døssing, L.N., Beukes, N.J., Bau, M., Kruger, S.J., Frei, R., Canfield, D.E., 2013. Atmospheric oxygenation three billion years ago. *Nature*, 501, 535-538.

Cullen, J.T., Coogan, L.A., 2017. Changes in Fe oxidation rate in hydrothermal plumes as a potential driver of enhanced hydrothermal input to near-ridge sediments during glacial terminations. *Geophysical Research Letters*, 44(23), 11-951.

Cutter, G. A., Casciotti, K., Croot, P., Geibert, W., Heimbürger, L. E., Lohan, M. C., Planquette, H., van de Flierdt, T, 2017. Sampling and Sample-handling Protocols for GEOTRACES Cruises, Version 3.0, Bremerhaven, GEOTRACES Standards and Intercalibration Committee.

Dideriksen, K., Baker, J.A., Stipp, S.L.S., 2008. Equilibrium Fe isotope fractionation between inorganic aqueous Fe (III) and the siderophore complex, Fe (III)-desferrioxamine B. *Earth and Planetary Science Letters*, 269(1-2), 280-290.

Døssing, L.N., Dideriksen, K., Stipp, S.L.S., Frei, R., 2011. Reduction of hexavalent chromium by ferrous iron: a process of chromium isotope fractionation and its relevance to natural environments. *Chemical Geology*, 285(1-4), 157-166.

Douville, E., Charlou, J.L., Oelkers, E.H., Bienvenu, P., Colon, C.J., Donval, J.P., Fouquet, Y., Prieur, D., Appriou, P., 2002. The Rainbow vent fluids (36°14'N, MAR): the influence of ultramafic rocks and phase separation on trace metal content in Mid-Atlantic Ridge hydrothermal fluids. *Chemical Geology*, 184(1-2), 37-48.

Elderfield, H., Schultz, A., 1996. Mid-ocean ridge hydrothermal fluxes and the chemical composition of the ocean. *Annual Review of Earth and Planetary Sciences*, 24(1), 191-224.

Evans, G.N., Seyfried, W.E., Tan, C., 2023. Nutrient transition metals in a time series of hydrothermal vent fluids from Main Endeavour Field, Juan de Fuca Ridge, Pacific Ocean. *Earth and Planetary Science Letters*, 602, 117943. DOI: 10.1016/j.epsl.2022.117943

Feely, R.A., Baker, E.T., Marumo, K., Urabe, T., Ishibashi, J., Gendron, J., Lebon, G.T., Okamura, K., 1996. Hydrothermal plume particles and dissolved phosphate over the superfast-spreading southern East Pacific Rise. *Geochimica et Cosmochimica Acta*, 60(13), 2297-2323.

Field, M.P., Sherrell, R.M., 2000. Dissolved and particulate Fe in a hydrothermal plume at 9°45' N, East Pacific Rise: Slow Fe (II) oxidation kinetics in Pacific plumes. *Geochimica et Cosmochimica Acta*, 64(4), 619-628.

Findlay, A.J., Estes, E.R., Gartman, A., Yücel, M., Kamyshny, A., Luther, G.W., 2019. Iron and sulfide nanoparticle formation and transport in nascent hydrothermal vent plumes. *Nature Communications*, 10(1), 1-7. DOI: 10.1038/s41467-019-09580-5

Fitzsimmons, J.N., Carrasco, G.G., Wu, J., Roshan, S., Hatta, M., Measures, C. I., Conway, T.M., John, S.G., Boyle, E.A., 2015. Partitioning of dissolved iron and iron isotopes into soluble and colloidal phases along the GA03 GEOTRACES North Atlantic Transect. *Deep Sea Research Part II: Topical Studies in Oceanography*, 116, 130-151.

Fitzsimmons, J.N., John, S.G., Marsay, C.M., Hoffman, C.L., Nicholas, S.L., Toner, B.M., German, C.R., Sherrell, R.M., 2017. Iron persistence in a distal hydrothermal plume supported by dissolved-particulate exchange. *Nature Geoscience*, 10(3), 195-201.

Frei, R., Gaucher, C., Poulton, S.W., Canfield, D.E., 2009. Fluctuations in Precambrian atmospheric oxygenation recorded by chromium isotopes. *Nature*, 461, 250-253.

Gartman, A., Findlay, A.J., Luther III, G.W., 2014. Nanoparticulate pyrite and other nanoparticles are a widespread component of hydrothermal vent black smoker emissions. *Chemical Geology*, 366, 32-41.

GEOTRACES Intermediate Data Product Group, 2021. The GEOTRACES Intermediate Data Product 2021 (IDP2021). NERC EDS British Oceanographic Data Centre NOC. DOI: 10.5285/cf2d9ba9-d51d-3b7c-e053-8486abc0f5fd

German, C.R., Campbell, A.C., Edmond, J.M., 1991. Hydrothermal scavenging at the Mid-Atlantic Ridge: modification of trace element dissolved fluxes. *Earth and Planetary Science Letters*, 107(1), 101-114.

González-Santana, D., González-Dávila, M., Lohan, M.C., Artigue, L., Planquette, H., Sarthou, G., Tagliabue, A., Santana-Casiano, J.M., 2021. Variability in iron (II) oxidation kinetics across diverse hydrothermal sites on the northern Mid Atlantic Ridge. *Geochimica et Cosmochimica Acta*, 297, 143-157.

González-Santana, D., Lough, A.J., Planquette, H., Sarthou, G., Tagliabue, A., Lohan, M.C., 2023. The unaccounted dissolved iron (II) sink: Insights from dFe (II) concentrations in the deep Atlantic Ocean. *Science of the Total Environment*, 862, 161179. DOI: 10.1016/j.scitotenv.2022.161179

Goring-Harford, H.J., Klar, J.K., Pearce, C.R., Connelly, D.P., Achterberg, E.P., James, R.H., 2018. Behaviour of chromium isotopes in the eastern sub-tropical Atlantic Oxygen Minimum Zone. *Geochimica et Cosmochimica Acta*, 236, 41-59.

Gueguen, B., Reinhard, C.T., Algeo, T., Peterson, L.C., Nielsen, S.G., Wand, X., Rowe, H., Planavsky, N.J., 2016. The chromium isotope composition of reducing and oxic marine sediments. *Geochimica et Cosmochimica Acta*, 184, 1-19.

Hoffman, C.L., Monreal, P.J., Albers, J.B., Lough, A.J., Santoro, A.E., Mellett, T., Buck, K., Tagliabue, A., Lohan, M., Bundy, R.M., 2023. Microbial siderophore production is tightly coupled to iron in hydrothermal plumes. *bioRxiv*, 2023-01. DOI: 10.1101/2023.01.05.522639

Holmden, C., Jacobson, A.D., Sageman, B.B., Hurtgen, M.T., 2016. Response of the Cr isotope proxy to Cretaceous Ocean Anoxic Event 2 in a pelagic carbonate succession from the Western Interior Seaway. *Geochimica et Cosmochimica Acta*, 186, 277-295.

Homoky, W.B., Conway, T.M., John, S.G., König, D., Deng, F., Tagliabue, A., Mills, R.A., 2021. Iron colloids dominate sedimentary supply to the ocean interior. *Proceedings of the National Academy of Sciences*, 118 (13). DOI: 10.1073/pnas.2016078118

Homoky, W.B., Severmann, S., Mills, R.A., Statham, P.J., Fones, G.R., 2009. Pore-fluid Fe isotopes reflect the extent of benthic Fe redox recycling: evidence from continental shelf and deep-sea sediments. *Geology*, 37(8), 751-754.

Huang, J., Hao, J., Huang, F., Sverjensky, D.A., 2019. Mobility of chromium in high temperature crustal and upper mantle fluids. *Geochemical Perspective Letters*, 12, 1-6. DOI: 10.7185/geochemlet.1926

Huang, T., Moos, S.B., Boyle, E.A., 2021. Trivalent chromium isotopes in the eastern tropical North Pacific oxygen-deficient zone. *Proceedings of the National Academy of Sciences*, 118(8). DOI: 10.1073/pnas.1918605118.

Janssen, D.J., Gilliard, D., Rickli, J., Nasemann, P., Koschinsky, A., Hassler, C.S., Bowie, A.R., Ellwood, M.J., Kleint, C., Jaccard, S.L., 2023. Chromium stable isotope distributions in the southwest Pacific Ocean and constraints on hydrothermal input from the Kermadec Arc. *Geochimica et Cosmochimica Acta*, 342, 31-44.

Janssen, D.J., Rickli, J., Abbott, A.N., Ellwood, M.J., Twining, B.S., Ohnemus, D.C., Nasemann, P., Gilliard, D., Jaccard, S.L., 2021. Release from biogenic particles, benthic fluxes, and deep water circulation control Cr and δ^{53}Cr distributions in the ocean interior. *Earth and Planetary Science Letters*, 574. DOI: 10.1016/j.epsl.2021.117163

Janssen, D.J., Rickli, J., Quay, P.D., White, A.E., Nasemann, P., Jaccard, S.L., 2020. Biological control of chromium redox and stable isotope composition in the surface ocean. *Global Biogeochemical Cycles*. DOI: 10.1029/2019GB006397

Janssen, D.J., Rickli, J., Wille, M., Sepúlveda Steiner, O., Vogel, H., Dellwig, O., Berg, J.S., Bouffard, D., Lever, M.A., Hassler, C.S., Jaccard, S.L., 2022. Chromium cycling in redox-stratified basins challenges δ^{53}Cr paleoredox proxy applications. *Geophysical Research Letters*, 49(21). DOI: 10.1029/2022GL099154

Kitchen, J.W., Johnson, T.M., Bullen, T.D., Zhu, J., Raddatz, A., 2012. Chromium isotope fractionation factors for reduction of Cr (VI) by aqueous Fe (II) and organic molecules. *Geochimica et Cosmochimica Acta*, 89, 190-201.

Klar, J.K., James, R.H., Gibbs, D., Lough, A., Parkinson, I., Milton, J.A., Hawkes, J.A., Connelly, D.P., 2017. Isotopic signature of dissolved iron delivered to the Southern Ocean from hydrothermal vents in the East Scotia Sea. *Geology*, 45(4), 351-354.

Kleint, C., Bach, W., Diehl, A., Fröhberg, N., Garbe-Schönberg, D., Hartmann, J.F., de Ronde, C.E., Sander, S.G., Strauss, H., Stucker, V.K., Thal, J., 2019. Geochemical characterization of highly diverse hydrothermal fluids from volcanic vent systems of the Kermadec intraoceanic arc. *Chemical Geology*, 528, 119289. DOI: 10.1016/j.chemgeo.2019.119289

König, D., Conway, T.M., Ellwood, M.J., Homoky, W.B., Tagliabue, A., 2021. Constraints on the cycling of iron isotopes from a global ocean model. *Global Biogeochemical Cycles*, 35(9). DOI: 10.1029/2021GB006968

Lough, A., Klar, J., Homoky, W., Comer-Warner, S., Milton, J., Connelly, D., James, R., Mills, R., 2017. Opposing authigenic controls on the isotopic signature of dissolved iron in hydrothermal plumes. *Geochimica et Cosmochimica Acta*, 202, 1-20.

Lough, A.J.M., Tagliabue, A., Demasy, C., Resing, J.A., Mellett, T., Wyatt, N.J., Lohan, M.C., 2023. Tracing differences in iron supply to the Mid-Atlantic Ridge valley between hydrothermal vent sites: implications for the addition of iron to the deep ocean. *Biogeosciences*, 20 (2), 405-420.

Middleton, J.L., Langmuir, C.H., Mukhopadhyay, S., McManus, J.F., Mitrovica, J.X., 2016. Hydrothermal iron flux variability following rapid sea level changes. *Geophysical Research Letters*, 43(8), 3848-3856.

Miletto, M., Wang, X., Planavsky, N.J., Luther, G.W., Lyons, T.W., Tebo, B.M., 2021. Marine microbial Mn (II) oxidation mediates Cr (III) oxidation and isotope fractionation. *Geochimica et Cosmochimica Acta*, 297, 101-119.

689 Moos, S.B., 2018. The marine biogeochemistry of chromium isotopes. *Doctoral dissertation,*
690 *Massachusetts Institute of Technology*. URI: http://hdl.handle.net/1721.1/115788

691 Moos, S.B., Boyle, E.A., 2019. Determination of accurate and precise chromium isotope ratios in
692 seawater samples by MC-ICP-MS illustrated by analysis of SAFe Station in the North Pacific
693 Ocean. *Chemical Geology*, 511, 481-493.

694 Moos, S.B., Boyle, E.A., Altabet, M.A., Bourbonnais, A., 2020. Investigating the cycling of
695 chromium in the oxygen deficient waters of the Eastern Tropical North Pacific Ocean and the
696 Santa Barbara Basin using stable isotopes. *Marine Chemistry*, 221, 103756. DOI:
697 10.1016/j.marchem.2020.103756

698 Morgan, J.L., Wasylenki, L.E., Nuester, J., Anbar, A.D., 2010. Fe isotope fractionation during
699 equilibration of Fe-organic complexes. *Environmental Science & Technology*, 44(16), 6095-6101.

700 Mottl, M. J., McConachy, T. F., 1990. Chemical processes in buoyant hydrothermal plumes on the
701 East Pacific Rise near 21°N. *Geochimica et Cosmochimica Acta*, 54(7), 1911-1927.

702 Nasemann, P., Gault-Ringold, M., Stirling, C.H., Koschinsky, A., Sander, S.G., 2018. Processes
703 affecting the isotopic composition of dissolved iron in hydrothermal plumes: A case study from
704 the Vanuatu back-arc. *Chemical Geology*, 476, 70-84.

705 Nasemann, P., Janssen, D.J., Rickli, J., Grasse, P., Frank, M., Jaccard, S.L., 2020. Chromium
706 reduction and associated stable isotope fractionation restricted to anoxic shelf waters in the
707 Peruvian Oxygen Minimum Zone. *Geochimica et Cosmochimica Acta*, 285, 207-224.

708 Pettine, M., D'ottone, L., Campanella, L., Millero, F. J., Passino, R., 1998. The reduction of
709 chromium (VI) by iron (II) in aqueous solutions. *Geochimica et Cosmochimica Acta*, 62(9), 1509-
710 1519.

711 Pöppelmeier, F., Janssen, D.J., Jaccard, S.L., Stocker, T.F., 2021. Modeling the marine chromium
712 cycle: New constraints on global-scale processes. *Biogeosciences*, 18(19), 5447-5463.

713 Resing, J. A., Mottl, M. J., 1992. Determination of manganese in seawater using flow injection
714 analysis with on-line preconcentration and spectrophotometric detection. *Analytical Chemistry*,
715 64(22), 2682-2687.

716 Rickli, J., Janssen, D.J., Hassler, C., Ellwood, M.J., Jaccard, S.L., 2019. Chromium
717 biogeochemistry and stable isotope distribution in the Southern Ocean. *Geochimica et*
718 *Cosmochimica Acta*, 262, 188-206.

719 Rouxel, O., Shanks, W.C., Bach, W., Edwards, K.J., 2008. Integrated Fe- and S-isotope study of
720 seafloor hydrothermal vents at East Pacific Rise 9-10°N. *Chemical Geology*, 252(3), 214-227.

721 Rouxel, O., Toner, B.M., Manganini, S.J., German, C.R., 2016. Geochemistry and iron isotope
722 systematics of hydrothermal plume fall-out at East Pacific Rise 9°50' N. *Chemical Geology*, 441,
723 212-234.

724 Rudnicki, M.D., Elderfield, H., 1993. A chemical model of the buoyant and neutrally buoyant
725 plume above the TAG vent field, 26 degrees N, Mid-Atlantic Ridge. *Geochimica et Cosmochimica*
726 *Acta*, 57(13), 2939-2957.

727 Saad, E.M., Wang, X., Planavsky, N.J., Reinhard, C.T., Tang, Y, 2017. Redox-independent
728 chromium isotope fractionation induced by ligand-promoted dissolution. *Nature Communications*,
729 8, 1-10. DOI: 10.1038/s41467-017-01694-y

730 Scheiderich, K., Amini, M., Holmden, C., Francois, R., 2015. Global variability of chromium
731 isotopes in seawater demonstrated by Pacific, Atlantic, and Arctic Ocean samples. *Earth and*
732 *Planetary Science Letters*, 423, 87-97.

733 Schoenberg, R., Zink, S., Staubwasser, M., von Blanckenburg, F., 2008. The stable Cr isotope
734 inventory of solid Earth reservoirs determined by double spike MC-ICP-MS. *Chemical Geology*,
735 249(3-4), 294-306.

736 Severmann, S., Johnson, C., Beard, B., German, C., Edmonds, H., Chiba, H., Green, D., 2004. The
737 effect of plume processes on the Fe isotope composition of hydrothermally derived Fe in the deep
738 ocean as inferred from the Rainbow vent site, Mid-Atlantic Ridge, 36°14′ N. *Earth and Planetary*
739 *Science Letters*, 225(1), 63-76.

740 Tagliabue, A., Aumont, O., Bopp, L., 2014. The impact of different external sources of iron on the
741 global carbon cycle. *Geophysical Research Letters*, 41(3), 920-926.

742 Tagliabue, A., Lough, A. J., Vic, C., Roussenov, V., Gula, J., Lohan, M. C., Resing, J.A., Williams,
743 R.G., 2022. Mechanisms driving the dispersal of hydrothermal iron from the northern Mid Atlantic
744 Ridge. *Geophysical Research Letters*, 49(22). DOI: 10.1029/2022GL100615

745 Trocine, R.P., Trefry, J.H., 1988. Distribution and chemistry of suspended particles from an active
746 hydrothermal vent site on the Mid-Atlantic Ridge at 26°N. *Earth and Planetary Science Letters*,
747 88(1-2), 1-15.

748 van der Weijden, C.H., Reith, M., 1982. Chromium (III)-chromium (VI) interconversions in
749 seawater. *Marine Chemistry*, 11(6), 565-572.

750 Wang, H., Wang, W., Liu, M., Zhou, H., Ellwood, M.J., Butterfield, D.A., Buck, N.J., Resing,
751 J.A., 2022. Iron ligands and isotopes in hydrothermal plumes over backarc volcanoes in the
752 Northeast Lau Basin, Southwest Pacific Ocean. *Geochimica et Cosmochimica Acta*, 336, 341-352.

753 Wang, W., Goring-Harford, H., Kunde, K., Woodward, E.M.S., Lohan, M.C., Connelly, D.P.,
754 James, R.H., 2023. Biogeochemical cycling of chromium and chromium isotopes in the sub-
755 tropical North Atlantic Ocean. *Frontiers in Marine Science*, 10, 1165304. DOI:
756 10.3389/fmars.2023.1165304

757 Wang, W., Lough, A., Lohan, M.C., Connelly, D.P., Cooper, M., Milton, J.A., Chavagnac, V.,
758 Castillo, A., James, R.H., 2021. Behavior of iron isotopes in hydrothermal systems: Beebe and
759 Von Damm vent fields on the Mid-Cayman ultraslow-spreading ridge. *Earth and Planetary*
760 *Science Letters*, 575. DOI: 10.1016/j.epsl.2021.117200

761 Welch, S., Beard, B., Johnson, C., Braterman, P., 2003. Kinetic and equilibrium Fe isotope
762 fractionation between aqueous Fe (II) and Fe (III). *Geochimica et Cosmochimica Acta*, 67(22),
763 4231-4250.

764 Wu, L., Beard, B.L., Roden, E.E., Johnson, C.M., 2011. Stable iron isotope fractionation between
765 aqueous Fe (II) and hydrous ferric oxide. *Environmental Science & Technology*, 45(5), 1847-1852.

766 Yobo, L.N., Holmden, C., Brandon, A.D., Lau, K.V., Eldrett, J.S., Bergman, S., 2022. LIP
767 volcanism (not anoxia) tracked by Cr isotopes during Ocean Anoxic Event 2 in the proto-North
768 Atlantic region. *Geochimica et Cosmochimica Acta*, 332, 138-155.

769

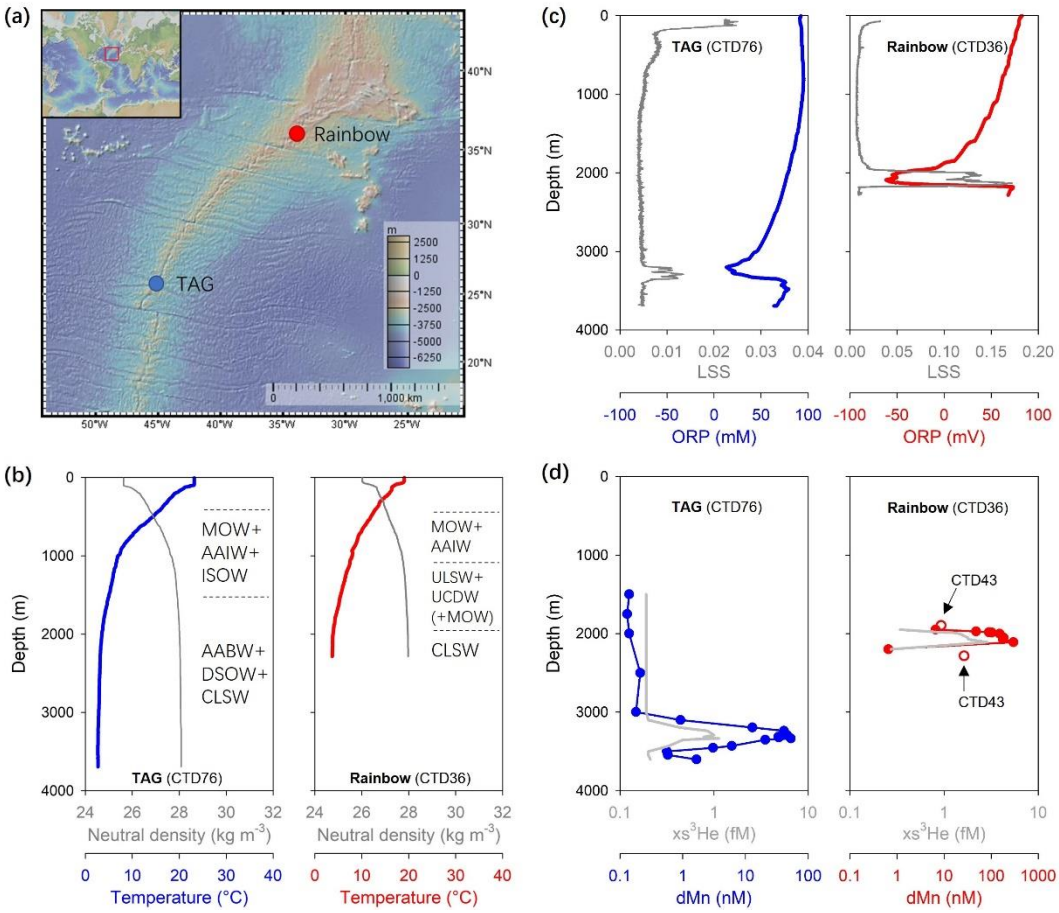

Figure 1 (a) Locations of sampling stations at the TAG and Rainbow hydrothermal sites on the MAR. Map courtesy of http://www.geomapapp.org **(b)** Full water column depth profiles of neutral density and temperature at TAG and Rainbow. Water masses (see Table S3) are delimited by horizontal dashed lines. MOW, Mediterranean Outflow Water; AAIW, Antarctic Intermediate Water; ISOW, Iceland Scotland Overflow Water; AABW, Antarctic Bottom Water; DSOW, Denmark Straits Overflow Water; CLSW, Classical Labrador Sea Water; ULSW, Upper Labrador Sea Water; UCDW, Upper Circumpolar Deep Water. **(c)** Full water column depth profiles of LSS and ORP. **(d)** Water column depth profiles of dissolved Mn and excess ^{3}He. Note that as helium was not sampled from the same cast as trace elements, it was calibrated using contemporaneous dMn values (*Lough et al., 2023*). At TAG, hydrothermal plume samples were collected from CTD 76; at Rainbow, plume samples were from CTD 36 and, additionally, from CTD 43 (Table S2, S3).

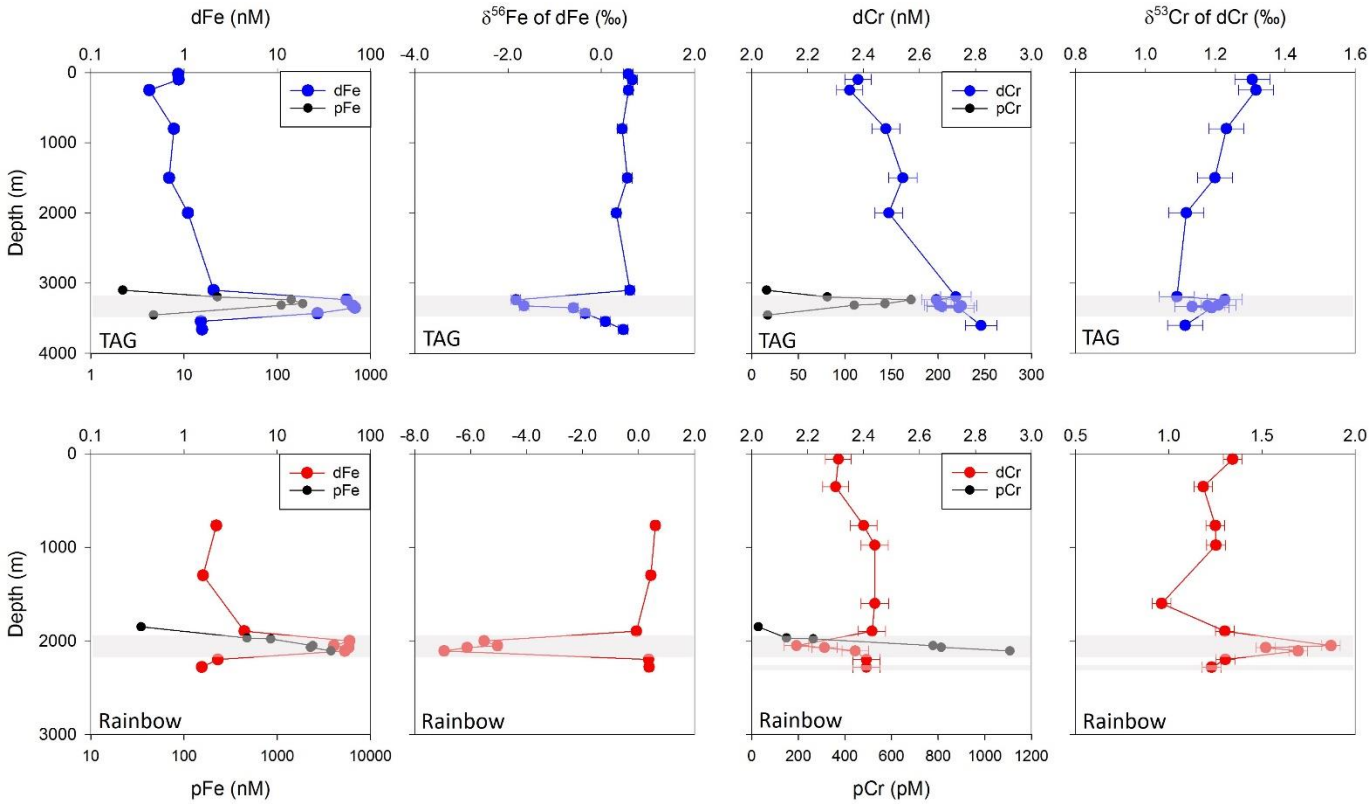

783

784 **Figure 2** Depth profiles of dissolved Fe and Cr concentrations, dissolved δ^{56}Fe and δ^{53}Cr values,
785 and particulate Fe and Cr concentrations at TAG (**top panels**) and Rainbow (**bottom panels**).
786 Locations of hydrothermal plumes are highlighted by the grey horizontal bands. Error bars for Fe
787 and Cr concentrations represent ±2% uncertainty; error bars for δ^{56}Fe and δ^{53}Cr represent external
788 reproducibility (±0.10‰ and ±0.06‰, respectively) based on repeat analyses of HEM and OSIL
789 samples. All data are given in the Supplementary Information (Tables S2 and S3).

790

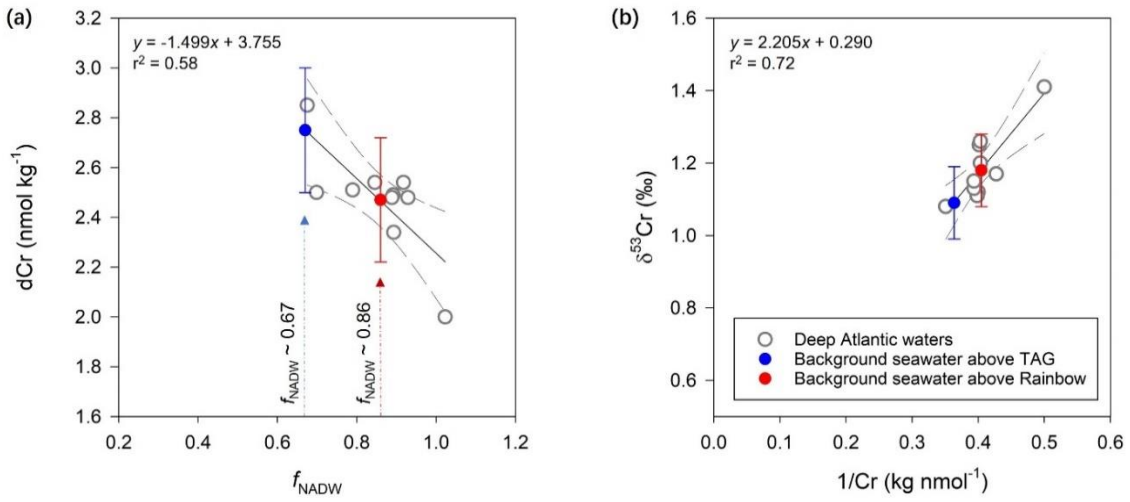

Figure 3 Relationships (significant at $p<0.05$; 95% confidence interval is shown by dashed lines) between (a) dCr and the fraction of NADW (f_{NADW}), and (b) δ^{53}Cr and 1/Cr in deep Atlantic waters (>2000 m, excluding samples collected from within 30 m of the seabed). Open circles represent literature data from *Goring-Harford et al. (2018)* and *Wang et al. (2023)*. Background seawater Cr concentrations and δ^{53}Cr values above the TAG and the Rainbow vent fields are estimated from their known water mass compositions (Table S3). The maximum uncertainties of the background values are ±0.25 nmol kg^{-1} for dCr and ±0.10‰ for δ^{53}Cr (1.96 times the Root Mean Square Error (RMSE) of the linear correlations).

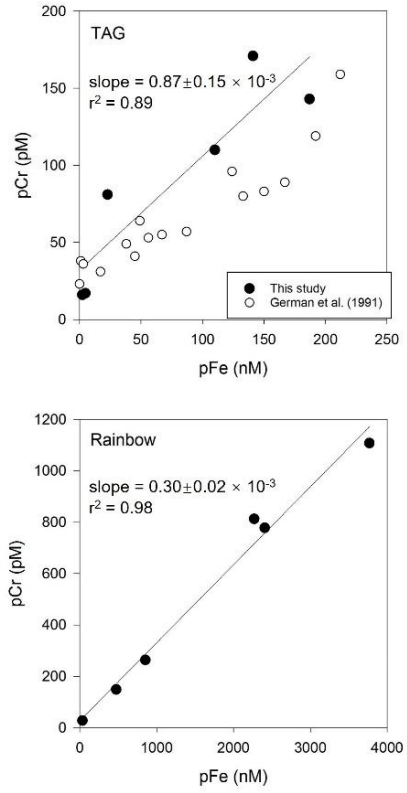

801

802 **Figure 4** Particulate Cr and particulate Fe concentrations for plume samples measured in this study,
803 together with samples collected from the TAG plume in 1988 reported in *German et al. (1991)*.

804

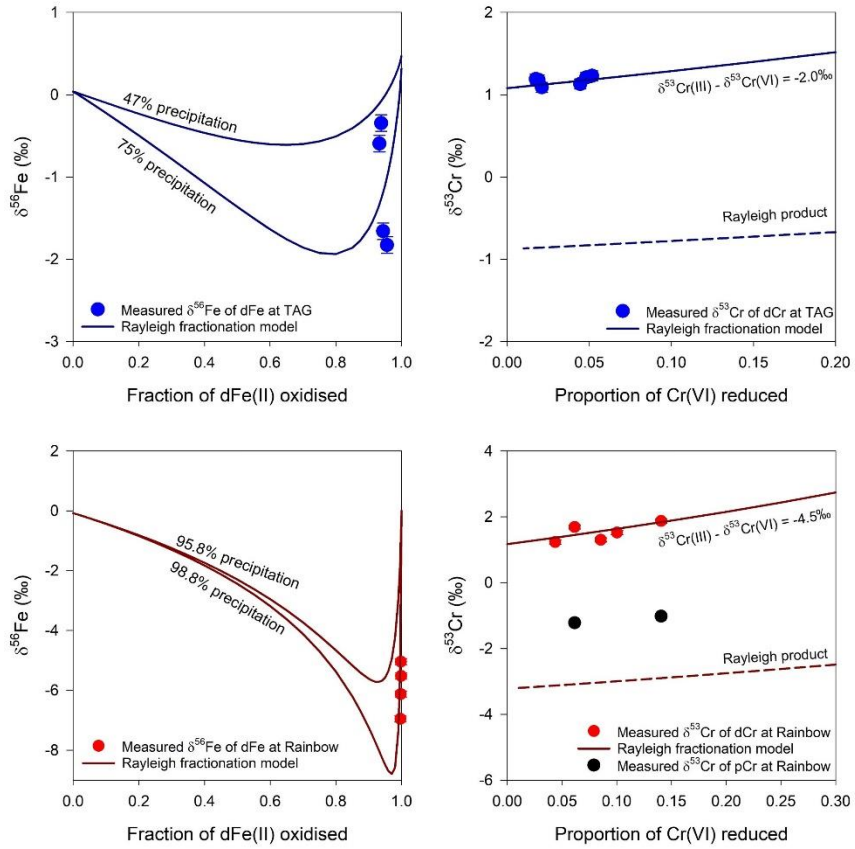

805

806 **Figure 5** Rayleigh models of Fe and Cr isotope fractionation in the TAG and Rainbow
807 hydrothermal plumes. **Left panels**: δ^{56}Fe versus the fraction of dFe(II) oxidised to Fe(III). Solid
808 lines show the evolution of dissolved δ^{56}Fe predicted by Rayleigh fractionation modelling of
809 Fe(II)-Fe(III) oxidation. Fractionation factor between aqueous Fe(II) and inorganic Fe(III), α_1, is
810 1.0035; fractionation factor between FeL and inorganic Fe(III), α_2, is 1.0006. Initial dFe(II) isotope
811 compositions are $\delta^{56}Fe(II)_0$ = 0.06‰ and −0.08‰ at TAG and Rainbow respectively. See Section
812 5.1 for details. **Right panels**: δ^{53}Cr relative to the proportion of Cr(VI) reduced to Cr(III) with
813 Fe(II). The solid line shows the evolution of dissolved δ^{53}Cr predicted by Rayleigh fractionation
814 modelling. Initial dCr isotope compositions are $\delta^{53}Cr_{sw}$ = 1.09‰ and 1.18‰ at TAG and Rainbow,
815 respectively. The Cr isotope fractionation factor between Cr(III) and Cr(VI) is estimated from the
816 correlation between the logarithmic dCr concentration and δ^{53}Cr (Section 5.2).

817

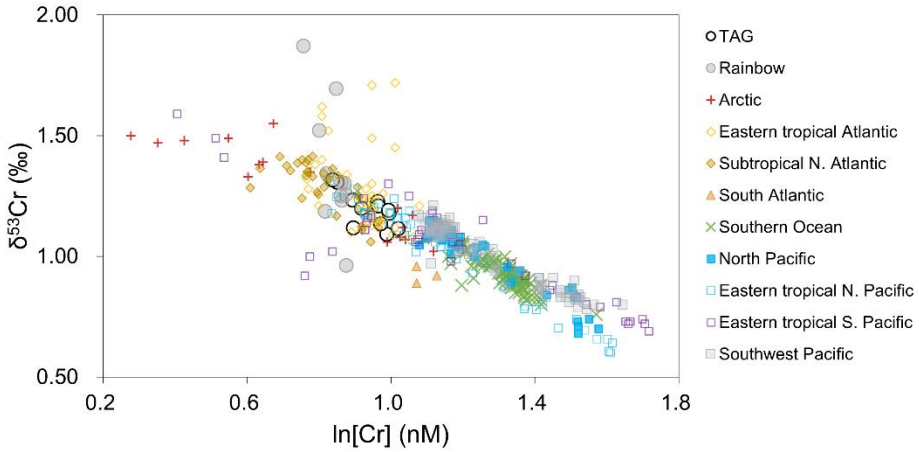

818

819 **Figure 6** Cross plot of dissolved $\delta^{53}Cr$ values versus logarithmic Cr concentration, for new data
820 from this study together with open ocean seawater data from the literature: *Scheiderich et al. (2015)*
821 (Arctic); *Goring-Harford et al. (2018)* (eastern tropical Atlantic); *Rickli et al. (2019)* (Southern
822 Ocean); *Moos & Boyle (2019)* (North Pacific); *Janssen et al. (2020)* (North Pacific); *Moos et al.*
823 *(2020)* (eastern tropical North Pacific); *Huang et al. (2021)* (eastern tropical North Pacific);
824 *Nasemann et al. (2020)* (eastern tropical South Pacific); *Janssen et al. (2021)* (Southern Ocean,
825 North Pacific, eastern tropical South Pacific, Southwest Pacific, South Atlantic); *Janssen et al.*
826 *(2023)* (Southwest Pacific); *Wang et al. (2023)* (subtropical North Atlantic).

827

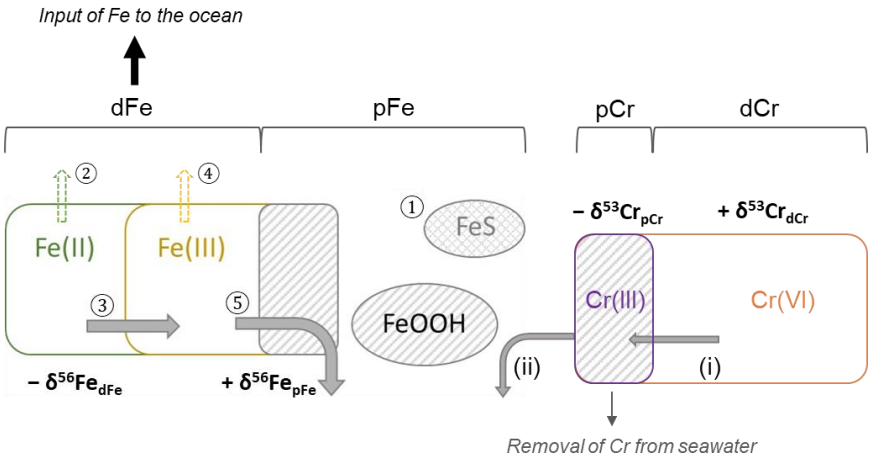

828

829 **Figure 7** Schematic showing the coupled cycling of Fe and Cr in the hydrothermal plume. ①
830 Precipitation of Fe-sulfide; ② Formation of nanoparticulate pyrite; ③ Oxidation of remaining
831 dissolved Fe(II) to Fe(III); ④ Complexation of part of the Fe(III) with organic ligands; ⑤
832 Precipitation of un-complexed Fe(III) as Fe-(oxyhydr)oxide. (i) Reduction of Cr(VI) to Cr(III); (ii)
833 Scavenging of Cr(III) onto Fe-(oxyhydr)oxide particles.

834

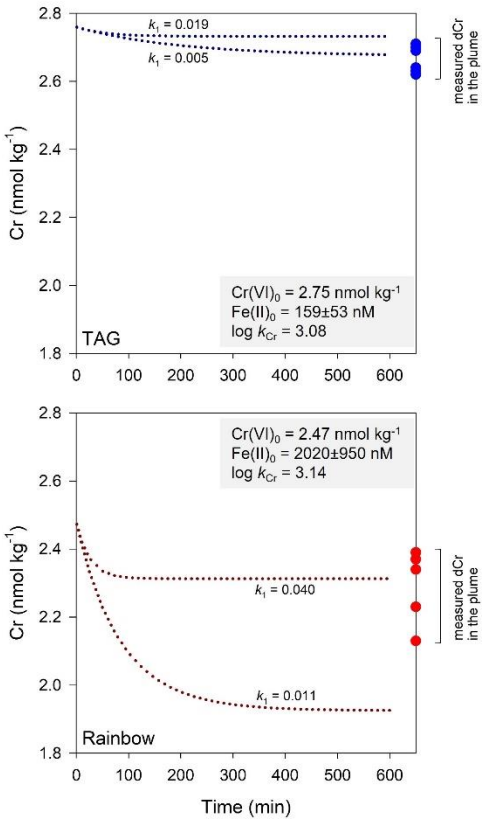

835

836 **Figure 8** Change in dissolved Cr concentration over time due to coupled Cr(VI) reduction and
837 Fe(II) oxidation (Section 5.3 and Supplementary Information S5). Dotted lines are the model
838 results; measured Cr concentrations in the TAG and Rainbow hydrothermal plumes are also shown.

839

Table 1. Parameters used to calculate estimated variables (*f*, *F* and *X*; Section 5.1) used to constrain the Rayleigh model for investigating the effects of precipitation of Fe-sulfides and Fe-(oxyhydr)oxides. dFe(II), dMn and TDFe data are from *Lough et al. (2023)* and *González-Santana et al. (2023)*. End-member vent fluid Fe and Mn concentrations are from *Chiba et al. (2001)* and *Douville et al. (2002)*; note, however, that the end-member metal concentrations may have evolved over the time.

	Measured parameters					Calculated parameters				
Depth (m)	δ^{56}Fe (‰)	dFe (nmol kg^{-1})	dFeII (nM)	dMn (nM)	TDFe (nM)	VF dilution factor	TDFe (nM)	*f* value Eq. 4	*F* value Eq. 9	*X* value Eq. 10
TAG (Station 35)										
End-member $[Fe]_{VF}$ = ~5170 µM, $[Mn]_{VF}$ = ~710 µM										
3236	-1.83	54.4	8.7	41.0	196	17000	298	66%	4.4%	25%
3322 **	-1.66	63.4	8.9	34.0	-	21000	246	65%	5.6%	36%
3350	-0.59	67.1	8.1	20.6	121	34000	150	81%	6.7%	53%
3429	-0.35	26.6	4.7	6.1	77 *	120000	44	-	6.2%	31%
Average					159±53 (1σ, n=2)			71±9% (1σ, n=3)		
Rainbow (Station 16)										
End-member $[Fe]_{VF}$ = ~24000 µM, $[Mn]_{VF}$ = ~2250 µM										
2001	-5.66	58.7	2.0	152	1360	15000	1620	84%	0.1%	4.2%
2051	-5.04	39.9	3.4	185	1630	12000	1970	83%	0.2%	2.3%
2072	-6.12	57.3	4.4	178	1660	13000	1900	87%	0.3%	3.2%
2108	-6.94	52.3	12.8	297	3430	7600	3170	108%	0.4%	1.2%
Average					2020±950 (1σ, n=4)			91±12% (1σ, n=4)		

*Not included in the calculation of average TDFe as this sample has a large dilution factor and is not representative of the earliest stages of plume dispersal. **No TDFe data are available for this sample, so TDFe is assumed to be equal to the average value.